

# G0.173-0.42: an X-ray and radio magnetized filament near the galactic center

F. Yusef-Zadeh<sup>1\*</sup>, M. Wardle<sup>2</sup>, C. Heinke<sup>3</sup>, I. Heywood<sup>4,5,6</sup>, R. Arendt<sup>7</sup>,

M. Royster<sup>1</sup>, W. Cotton<sup>8</sup>, F. Camilo<sup>6</sup> & J. Michail<sup>1</sup>

<sup>1</sup>*CIERA, Department of Physics and Astronomy Northwestern University, Evanston, IL 60208*

<sup>2</sup>*Dept of Physics and Astronomy, Research Centre for Astronomy, Astrophysics and Astrophotonics, Macquarie University, Sydney NSW 2109, Australia*

<sup>3</sup>*Dept of Physics, University of Alberta, CCIS-4-183, Edmonton, AB T6G 2E1, Canada*

<sup>4</sup>*Astrophysics, Department of Physics, University of Oxford, Keble Road, Oxford, OX1 3RH, UK*

<sup>5</sup>*Department of Physics and Electronics, Rhodes University, PO Box 94, Makhanda, 6140, South Africa*

<sup>6</sup>*South African Radio Astronomical Observatory, 2 Fir Street, Black River Park, Observatory, Cape Town, 7925, South Africa*

<sup>7</sup>*UMBC/GSFC/CRESST 2, Code 665, NASA/GSFC, 8800 Greenbelt Rd, Greenbelt MD 20771*

<sup>8</sup>*National Radio Astronomy Observatory, Charlottesville, VA, USA*

Accepted XXX. Received YYY; in original form ZZZ

## ABSTRACT

The recent detection of an X-ray filament associated with the radio filament G0.173 – 0.42 adds to four other nonthermal radio filaments with X-ray counterparts, amongst the more than 100 elongated radio structures that have been identified as synchrotron-emitting radio filaments in the inner couple of degrees of the Galactic center. The synchrotron mechanism has also been proposed to explain the emission from X-ray filaments. However, the origin of radio filaments and the acceleration sites of energetic particles to produce synchrotron emission in radio and X-rays remain mysterious. Using MeerKAT, VLA, *Chandra*, *WISE* and *Spitzer*, we present structural details of G0.173-0.42 which consists of multiple radio filaments, one of which has an X-ray counterpart. A faint oblique radio filament crosses the radio and X-ray filaments. Based on the morphology, brightening of radio and X-ray intensities, and radio spectral index variation, we argue that a physical interaction is taking place between two magnetized filaments. We consider that the reconnection of the magnetic field lines at the interaction site leads to the acceleration of particles to GeV energies. We also argue against the synchrotron mechanism for the X-ray emission due to the short  $\sim 30$  year lifetime of TeV relativistic particles. Instead, we propose that the inverse Compton scattering mechanism is more likely to explain the X-ray emission by upscattering of seed photons emitted from a  $10^6 L_{\odot}$  star located at the northern tip of the X-ray filament.

**Key words:** accretion, accretion disks — black hole physics — Galaxy: center

## 1 INTRODUCTION

More than 30 years have elapsed since the nonthermal radio filaments associated with the Galactic center radio Arc near  $l \sim 0.2^{\circ}$  were first reported (Yusef-Zadeh, Morris & Chance 1984). These observations showed linear, magnetized features running perpendicular to the Galactic plane and since then more than 100 nonthermal radio filaments (NRFs) with similar characteristics have been discovered (Liszt 1985; Yusef-Zadeh 1986; Morris & Yusef-Zadeh 1989; Gray, et al. 1991; Haynes, et al. 1992; Lang, Morris & Echevarria 1999; LaRosa, et al. 2004; Yusef-Zadeh, Hewitt & Cotton 2004; Law, Yusef-Zadeh & Cotton 2008; Heywood, et al. 2019). The intrinsic polarization observed from these filaments shows that their magnetic fields are directed along the filaments (Yusef-Zadeh,

Wardle & Parastaran 1997; Paré, et al. 2019). The mechanisms responsible for accelerating particles to relativistic energies and for creating the elongated filamentary geometry are still mysterious. While several authors have examined how the filaments might arise from their interaction with molecular and ionized clouds or with mass-losing stars there is no consensus on any model (Rosner & Bodo 1996; Shore & LaRosa 1999; Bicknell & Li 2001; Yusef-Zadeh & Wardle 2019).

*Chandra*, *XMM* and *NuSTAR* have detected X-ray emission from a handful of nonthermal radio filaments. There are four prominent radio and X-ray filaments that have been studied in detail, G359.89–0.08 (Sgr A-E), G359.54+0.18 (ripple), G359.90–0.06 (Sgr A-F), G0.13–0.11, Sakano, et al. (2003); Lu, Wang & Lang (2003); Lu, Yuan & Lou (2008); Yusef-Zadeh, et al. (2005); Zhang, et al. (2014, 2020). Unlike the long and distinct radio filaments, there are also several short,

\* E-mail: zadeh@northwestern.edu

linear X-ray features that are identified in the inner 6′ of Sgr A\* (Muno, et al. 2008; Johnson, Dong & Wang 2009; Lu, Yuan & Lou 2008). No detailed, high-resolution studies of the radio counterparts to these X-ray filaments have been published. In all previous studies, the synchrotron scenario for the X-ray emission has been proposed with the exception of G359.90-0.06 (Sgr A-F) which could be explained either by synchrotron or the inverse Compton scattering (ICS) (Yusef-Zadeh, et al. 2005). There are limited studies investigating the spectrum of the emission between radio and X-rays to determine the emission mechanism in radio and X-rays (Yusef-Zadeh, et al. 2005). Furthermore, the origin of X-ray filaments in many studies are speculated to be traces of pulsar wind nebulae associated with pulsars (Lu, Wang & Lang 2003; Lu, Yuan & Lou 2008; Zhang, et al. 2020).

Here we focus on a newly discovered source, an X-ray counterpart Zhang, Wang, & Clavel (2020) to the radio filament G0.173-0.42, which is also called G0.17-0.42 or S5 in (Yusef-Zadeh, Hewitt & Cotton 2004). This prominent radio filament lies towards eastern boundary of a diffuse, large-scale linearly polarized plume-like structure that runs toward negative latitudes of the Galactic plane (Yusef-Zadeh 1986; Yusef-Zadeh, et al. 1990; Seiradakis, et al. 1985; Tsuboi, et al. 1995; Yusef-Zadeh, Hewitt & Cotton 2004). G0.173-0.42 consists of two parallel filaments with an extent of  $\sim 11'$  oriented perpendicular to the Galactic plane (Yusef-Zadeh, Hewitt & Cotton 2004). We present X-ray observations of this filament indicating X-ray emission with an extent of  $\sim 2'$  along the radio filament.

A faint oblique radio filament crosses the radio and X-ray filament. We suggest that the acceleration of relativistic particles to GeV energies occurs due to reconnection of the magnetic fields at the location where the oblique filament crosses G0.173-0.42. We argue that the flow from the acceleration site encounters a luminous mass-losing star, thus the flow wraps around the mass-losing envelope of the star before it continues to the south. In this picture, the ICS is generating X-ray emission.

## 2 OBSERVATIONS AND DATA REDUCTION

### 2.1 VLA radio observations

Radio continuum observations at 20 and 6cm (project AY15) were carried out using the VLA in its hybrid BnC- and CnD-array configurations on October 6, 1986 and February 7, 1987, respectively. These scaled-array observations were made to determine the spectral index of G0.173-0.42. These observation were carried out in full polarization and narrow  $2 \times 50$  MHz band. We used 3C286 to calibrate the flux density scale, and 1748-253 to calibrate the complex gains. We used three overlapping 6cm fields; we are focusing on one 6cm field where X-ray emission is detected. The pointing centers at nominal frequencies at 4.80 and 1.47 GHz are  $\alpha, \delta(J2000) = 17^h 47^m 20^s .723, -28^\circ 59' 23'' .362$  and  $\alpha, \delta(J2000) = 17^h 47^m 40^s .768, -29^\circ 01' 00'' .806$ , respectively.

### 2.2 MeerKAT radio observations

The Galactic center region was observed by MeerKAT as part of its commissioning phase. The pointing used here was ob-

served for 10.8 hours on 15 June 2018, with the array pointing at  $\alpha, \delta(J2000) = 17^h 47^m 38^s .34, -29^\circ 06' 18'' .95$ , for an on-source time of 6.84 hours. A full overview of the project will be provided by Heywood et al. (in prep.), however a brief description of the major data processing steps are as follows. Averaging was applied to the data to reduce the native 4,096 channels by a factor of 4. Basic flagging commands were applied using the `flagdata` task in CASA including bandpass edges and regions of persistent radio frequency interference. Delay and bandpass corrections were derived from observations of the primary calibrator source PKS B1934-638, which was also used to set the absolute flux scale. Time-dependent gains were derived from observations of a bright (8 Jy at 1.28 GHz) calibrator source 1827-360, which was observed for 1 minute for every 10 minute target scan. Gain corrections were derived iteratively with rounds of residual flagging in between. Following the application of these corrections, the target data were flagged using the `tricolour` package<sup>1</sup>, and then imaged using `wsclean` (Offringa et al. 2014) with multiscale cleaning (Offringa & Smirnov 2017) and iterative threshold-based masking. Phase-only self-calibration solutions were derived for every 128 seconds of data using the `gaincal` task in CASA, and the imaging process was repeated. A Briggs (1995) robustness parameter of  $-1.5$  was used to provide high angular resolution. The primary beam attenuation was corrected for by dividing the image by an azimuthally-averaged Stokes I beam model evaluated at 1.28 GHz using the `eidors` software (Asad et al. 2019).

The spectral index  $\alpha$ , is defined as  $I_\nu \propto \nu^\alpha$  where  $I_\nu$  is the intensity. Fifteen narrow channels within the broad 20 cm band were used to accurately determine the spectral index distribution. The procedure to make a spectral index image is as follows. Imaging the data in 15 sub-bands follows the application of a Gaussian taper to the visibilities of each sub-band to attempt to force common angular resolution. An inner cut to the  $u, v$  plane is also applied, to prevent the lowest frequencies seeing large angular scales that are not visible at higher frequencies. Each sub-image is primary beam corrected, and convolved with a circular Gaussian with a FWHM  $\sim 8''$ . The primary beam corrected, common resolution images are stacked into a cube, which is then masked below a threshold  $\sim 1$  mJy. A linear fit for the gradient of the spectrum is made in log-frequency/log-flux space for every sight line through the masked cube for which more than 50% of the frequency planes contain total intensity measurements.

### 2.3 Chandra X-ray observations

We use data from three *Chandra X-ray Observatory* observations, ObsIDs 7157 (14.9 ks), 19448 (44.5 ks), and 20111 (14.9 ks). Each observation used the Advanced CCD Imaging Spectrometer (ACIS) in the ACIS-I configuration. The data were processed using the *Chandra X-ray Center's* CIAO software package. We created images using exposure maps that divide out the instrument effective area in a variety of energy ranges, and eventually adopted 1.5-8 keV to create images (see Figs. 1b,d and 4a). We show images smoothed with a Gaussian

<sup>1</sup> <https://github.com/ska-sa/tricolour>

with FWHM =  $4'' \times 4''$ . The CIAO software `vtpdetect` detects the filament with a false alarm probability of  $2 \times 10^{-33}$ . The filament is oriented at 2 degrees clockwise of north-south in Galactic coordinates. The filament seems to extend for at least  $100''$  ( $b = -00^\circ 26' 00''$  to  $b = -00^\circ 24' 15''$ ). It may extend farther to Galactic north and Galactic south.

Inspection of the merged image suggests that the filament shows three parts with different fluxes, which we designate North, South, and Center. The Center portion has the highest flux per unit area. A possible point source may be present at  $l = 00^\circ 10' 25''.61$   $b = -00^\circ 25' 15''.99$ . We extract spectra from the filament around this spot, designating it the Center region, and from the filament on either side of it. We use extraction regions  $7''$  in width, and with lengths  $58.2''$ ,  $5.7''$ , and  $41.7''$ , for the North, Center, and South portions respectively. Background regions are extracted from regions of similar width and length offset to either side of the filament by  $\sim 10''$ . The total number of counts in each region is 279, 42, and 138 counts respectively. After background subtraction, we infer  $260 \pm 23$  counts altogether can be attributed to the filament.

We fit the spectrum of the filament as a whole, and separately as three individual parts, using XSPEC version 12.10.1f. We do not combine spectra, but fit them together in XSPEC, tying parameters when appropriate (thus, all parameters are tied between epochs when fitting the spectrum of the whole filament). We fit power-law and thermal bremsstrahlung spectra, with interstellar absorption represented by the `tbabs` model assuming the `wilm` interstellar abundances of Wilms et al. (2001). Due to the small number of counts, we bin the data to 1 count/bin and fit using the C-statistic.

For the full spectrum fit with a power-law, we find best-fit values of  $N_H = 12_{-6}^{+10} \times 10^{22} \text{ cm}^{-2}$ , photon index  $\Gamma = 2.5_{-1.2}^{+1.7}$ , and 2-10 keV fluxes of (unabsorbed)  $2.0_{-0.5}^{+2.5} \times 10^{-13} \text{ ergs s}^{-1} \text{ cm}^{-2}$ , or (absorbed)  $1.0_{-0.3}^{+0.2} \times 10^{-13} \text{ ergs s}^{-1} \text{ cm}^{-2}$ . Extrapolating this fit to 0.5-10 keV, we find an unabsorbed flux of  $5.5 \times 10^{-13} \text{ ergs s}^{-1} \text{ cm}^{-2}$  (the high absorption and uncertainty in photon index make the intrinsic flux below 2 keV poorly constrained). Simulating 1000 fake datasets using the `goodness` command, we find that 20% give smaller test statistic values (using the Cramer-von Mises statistic), so the power-law model is acceptable.

We also test a thermal bremsstrahlung model, for which we find  $N_H = 12_{-6}^{+10} \text{ cm}^{-2}$ ,  $kT = 5_{-3}^{+81} \text{ keV}$ , and unabsorbed (absorbed) 2-10 keV flux of  $1.7_{-0.4}^{+0.8} \times 10^{-13}$  ( $1.0_{-0.2}^{+0.1} \times 10^{-13}$ )  $\text{ergs s}^{-1} \text{ cm}^{-2}$ . As the goodness for the bremsstrahlung fit is 24%, we cannot discriminate between these two models.

Fitting the three spatial parts of the X-ray filament with a power-law, we try either tying  $N_H$  and  $\Gamma$  between the parts, or just tying  $N_H$ . For the model with tied  $\Gamma$ , we find 2-10 keV unabsorbed fluxes of  $1.4_{-0.4}^{+1.6} \times 10^{-13}$ ,  $0.2_{-0.1}^{+0.3} \times 10^{-13}$ , and  $0.4_{-0.2}^{+0.6} \times 10^{-13} \text{ ergs s}^{-1} \text{ cm}^{-2}$ , for the North, Center and South portions respectively. If the power-law indices are freed, we find values of  $\Gamma = 2.9_{-1.4}^{+1.8}$ ,  $2.5_{-2.0}^{+2.2}$ , and  $1.8_{-1.8}^{+1.9}$  for the North, Center, and South portions respectively. We thus cannot distinguish whether there is any variation in power-law index among the three components.

#### 2.4 2MASS, Spitzer and WISE

In addition to radio and X-ray data, we have also examined 2MASS, *Spitzer* (IRAC and MIPS) and *WISE* images and

point source catalogs of the Galactic center (Skrutskie, et al. 2006; Stolovy, et al. 2006; Ramirez, et al. 2008; Yusef-Zadeh, et al. 2009). We employed these data to investigate the SEDs of sources that appear to be associated with filaments.

### 3 RESULTS

#### 3.1 Morphology

Figure 1 shows a close-up view of G0.173-0.42 in four different panels at 20 cm, 2-8 keV,  $3.6 \mu\text{m}$  and composite 3-color image of radio, X-ray and infrared. Figure 1a shows the eastern filament with a peak flux density of  $\sim 0.75 \text{ mJy beam}^{-1}$  at the position A,  $l = 10' 24.3''$ ,  $b = -24' 53.70''$ , where the oblique filament crosses the parallel filaments ("A" is defined as the intersection of the eastern filament with the oblique filament). When compared to typical surface brightness of G0.173-0.42, the intensity of the eastern filament increases by a factor of 2-3 near position A. Enhanced radio emission extends to both north and south of position A along the eastern filament. Figure 1b shows the X-ray emission near position A traces enhanced radio emission along the eastern filament.

At its north end, the X-ray filament deviates to the northeast and breaks up into two filaments. This is coincident with a luminous infrared star located at  $l = 10' 18''.81$ ,  $b = 23' 44''.61$  (circled in the  $3.6 \mu\text{m}$  image in Figure 1c). The star may be the brightest member of a cluster. The candidate cluster is defined by the 6 stars with  $[3.6] < 8.5 \text{ mag}$  that are located within  $20''$  of the bright star. There are no other groupings as bright and dense as this within  $200''$ , implying a less than 1% chance that the candidate cluster is simply a random arrangement of stars on the line of sight. The X-ray filament deviates to the northeast and breaks up into diffuse circular-shaped structure where a stellar cluster at  $3.6 \mu\text{m}$  is found. Figure 1d shows a composite image revealing that the northern tip of X-ray filament has no radio counterpart but coincides with the  $3.6 \mu\text{m}$  emission from the stellar cluster.

The comparison of radio and X-ray images shows that the X-ray counterpart to G0.173-0.42 lies to the east of the radio filament and the western radio filament has no X-ray counterpart (see Fig. 1c). We have not astrometrically corrected the radio and X-ray images to each other. The 90% uncertainty absolute astrometry errors for Chandra data are  $0.8''^2$ , while radio interferometric astrometric errors are comparably negligible. For the VLA, the astrometric accuracy is usually down to a few percent of the beamsize. MeerKAT data give systematic errors up to an arcsecond. A shift of  $1''$  (arcsecond) in the X-ray or radio positions would not affect the relative alignment of the filaments which are several arcseconds across.

The X-ray filament has a length of  $\sim 2' - 2.5'$ , far less than the radio filament that extends for  $\sim 11'$  (Yusef-Zadeh, Hewitt & Cotton 2004). A second filament also runs parallel to G0.173-0.42 and the two filaments extend for a total of  $\sim 20'$  (or 48pc at the 8 kpc Galactic center distance), as shown in Figure 2. We note that the strongest emission in Figure 2 arises from G0.173-0.42 where X-ray emission is detected. Lastly, the northern tip of the X-ray filament near

<sup>2</sup> <https://cxc.cfa.harvard.edu/cal/ASPECT/celmon/>

$b \sim -23' 45''$  deviates from radio filaments that themselves bend at Galactic latitude  $b \sim -23'$  by about 6 *arcdeg* to the northwest. The high resolution MeerKAT 20 cm image of G0.173-0.42 reveals the east and west filaments have the appearance of winding about each other and converging to the south near  $b \sim -27'$ . We note a third filament G0.167-0.405 crossing G0.173-0.42 at position A at an oblique angle of  $-32^\circ$ . The intensity of radio emission is stronger by a factor 2-3 to the south of A when compared to the north of A. As described below, radio spectrum becomes increasingly flatter to the south of position A.

Figures 1b and 1d show the X-ray filament encounters the stellar cluster. It appears that the northern extension of the X-ray filament from position A splits and wraps around the brightest member of the cluster and continues as two faint parallel linear features before the emission is terminated. We consider below that there is a physical interaction of the X-ray filament with the envelope this (presumed) mass-losing luminous star. Figure 3 shows the SED of the bright star derived from 2MASS, IRAC, MIPS *WISE* data. This star IRAC flux densities near or above the expected saturation limits. A fit to the 2MASS and *WISE* SED is also shown. Using the *WISE* data (black squares) instead of the saturated *Spitzer* IRAC data (open circles), the SED suggests about 2 mag extinction at K band with the corrected SED (red squares) characterized by a best fit stellar atmosphere model (blue stars) of  $T = 9250$  K, and an absolute K band magnitude of  $\sim 10.9$ . The extinction and absolute magnitude are derived using the Galactic center interstellar extinction law of Nishiyama et al. (2009). It may be that this source is intrinsically hot, but we can not rule out the possibility that there is a systematic error in the temperature derivation. This error could result from using a subset of the available model atmosphere parameters or the possible presence of warm dust that adds to the stellar emission at wavelengths as short as  $3.4 \mu\text{m}$ . The high temperature and the luminosity could be matched by a young massive star.

As the northern extension of the X-ray filament from position A crosses the cluster of stars, it does not follow the eastern radio filament. To demonstrate this, Figure 4 compares the intensity in radio and X-rays along three background subtracted slices across the width of the filaments, as labeled by horizontal lines on an X-ray image. The eastern filament has an X-ray counterpart. However, the separation of the peak emission from the radio filament with respect to its X-ray counterpart increases to the north is shown in Figure 4b (slice 3).

### 3.2 Radio and X-ray spectrum of G0.173-0.42

The spectral index  $\alpha$  of G0.173-0.42 is determined by measuring the flux density  $F_\nu$  at 15 frequency channels within the broad 20 cm bandwidth, as shown in Figure 5a. G0.173-0.42 shows a north-south gradient with the steepest and flattest spectral indices of  $\alpha \sim -1$  and  $\sim -0.2$  at the northern and southern ends of the parallel filaments, respectively. The eastern and western filaments are closer together to the south, as seen on Figures 1a and 2, where the flattest spectral index is noted. Furthermore, the emission is strongest south of position A. It is possible that enhanced brightening and flatter spectral index are due to a new generation of energetic parti-

cles that are accelerated at the interaction site, as discussed below.

In a close-up view of the region near position A, a change in the spectral index is noted exactly where the X-ray filament lies. To illustrate this, Figure 5b shows the spectral index determined from a slice cutting across the width of the filament. The eastern and western filaments show a flattening of  $\alpha \sim 0.3 - 0.35$  with respect to background emission with steeper spectrum. The intensity of 1631.6 MHz emission from a narrow channel is also plotted in Figure 5b.

Figure 6 shows a plot of radio and X-ray flux and their corresponding spectral indices. The integrated flux densities of the entire X-ray filament and the corresponding radio counterpart at 1.28 GHz are shown. The extrapolations of the radio and X-ray spectra are shown in red and blue, respectively, with dashed lines and shaded regions indicate the best fit spectral indices and their 90% confidence intervals. The 90% confidence level on the radio spectral index is computed from  $-1.18 \pm 0.16$  with a flux density of 75.5 mJy.

## 4 DISCUSSION

The increase in the X-ray and radio brightness of eastern filament at the location where the oblique filament crosses G0.173-0.42 suggests that the oblique filament is physically interacting with the parallel filaments. This is also supported by the observation that the oblique filament becomes fainter and wider from SE to NW as it crosses the parallel filaments.

We also note that the spectral index of radio emission is flatter to the south along the radio/X-ray filaments than to the north of the filament. This suggests that a new population of GeV electrons is injected where the oblique filament crosses the parallel filaments.

### 4.1 A model of X-ray and radio emission

#### 4.1.1 Galactic wind

Recent detection of large scale X-ray and synchrotron emission above and below the central molecular zone (CMZ) was interpreted as arising from cosmic-ray driven outflow (Yusef-Zadeh & Wardle 2019). In this picture, the cosmic-ray momentum and energy are mediated by the magnetic field and transferred to accelerating and heating the gas. The cosmic rays and heated gas open a channel away from the Galactic plane and expand as a Galactic wind. The interaction of this wind with any compact obstacles such as stellar wind bubbles creates the radio filaments which are analogous to cometary tails behind mass-losing stars like Mira-type stars (Martin et al. 2007). In the case of G0.173-0.42, the Galactic center wind is expected to flow towards more negative latitudes, away from the Galactic plane. A schematic diagram of this picture is shown in Figure 7.

#### 4.1.2 Interaction of two filaments: magnetic reconnection

Because of the morphological evidence of the physical interaction of the oblique and north-south nonthermal radio filaments, it is plausible that reconnection of their magnetic field lines generates a new population of energetic particles. This population is responsible not only for the sudden increase in

radio emission but also X-ray emission from G0.173-0.42 at point A.

The 1.2 GHz radio continuum emission along the eastern filament brightens to the South of point A, where it is crossed by the oblique filament. This brightening is accompanied by the flattening of the spectrum, from  $\sim \nu^{-1.4}$  to North of A, to  $\nu^{-0.5}$  to the South. The profile of the oblique filament becomes more diffuse and complex as it crosses the vertical filament at A. Together, these changes point to a physical interaction of the filaments at position A suggestive of the acceleration of electrons at A. One possible form of this interaction is magnetic reconnection. In this case, some of the dissipated magnetic energy is transferred to a new population of relativistic electrons. To estimate the available magnetic power we adopt a nominal field strength  $B = 100 \mu\text{G}$  (Yusef-Zadeh, et al. (2005); Yusef-Zadeh & Wardle (2019)), reconnection speed  $v = 20 \text{ km/s}$ , and cross-sectional area  $A = (0.2 \text{ pc})^2$ . Then the reconnection gives a power,  $L_r \sim v_A A B^2 / 8\pi \approx 3 \times 10^{32} \text{ erg s}^{-1}$ , and the lifetime of the interaction is of order the filament width,  $0.2 \text{ pc}$ , divided by the reconnection speed,  $20 \text{ km s}^{-1}$ , i.e.  $\sim 10^4$  years.

The energy of the electrons dominating the emission at 1.2 GHz is  $\sim 0.9 \text{ GeV}$ , and their synchrotron lifetime is  $\sim 0.9 \text{ Myr}$ . The enhanced radio emission associated with this population extends  $\approx 2 \text{ pc}$  to the south. If this were determined by the synchrotron lifetime, then their propagation speed would only be  $\sim 2 \text{ km s}^{-1}$ , an order of magnitude below the  $\sim 20 \text{ km s}^{-1}$  cosmic-ray streaming speed that is commonly inferred elsewhere. Instead, the spatial extent of the enhanced continuum emission is likely set by the time elapsed since the interaction between the filaments commenced. If the total interaction time scale between the filament is  $10^4 \text{ yr}$ , as estimated above, then the age of the electrons must be less than this, suggesting a propagation speed in excess of  $200 \text{ km s}^{-1}$ . This is far higher than the speeds associated with cosmic-ray streaming.

This is consistent with a model in which non-thermal filaments at the Galactic center are a result of a large-scale cosmic-ray driven wind (Yusef-Zadeh & Wardle 2019). In this picture a net flow of plasma away from the galactic plane at hundreds of  $\text{km s}^{-1}$  is driven by the extreme cosmic-ray pressure in the central  $150 \text{ pc}$  of the Galaxy (Oka, et al. 2019). The nonthermal filaments are magnetized streamers created by the wrapping of the wind's magnetic field around an obstacle to the flow, by analogy with the magnetized ion tails of comets embedded in the solar wind. The relativistic electrons injected by reconnection are advected by this flow, and the time to be transported from the injection point A to the southern tip of the radio-brightened portion for the filament is a few thousand years, consistent with the expected interval since the interaction between the two filaments began.

#### 4.1.3 Enhanced X-ray emission: ICS

We now turn to the origin of the X-ray emission. This is unlikely to be synchrotron emission for three reasons. First, the distribution does not match that of the brighter, flat spectrum radio emission, but extends a couple of pc to the north and south of the injection point A. Second, the lifetime of the  $\sim 30 \text{ TeV}$  electrons that would radiate in the keV range via synchrotron emission would be only 30 years, implying that their propagation speed to the north and south from the in-

jection point would need to exceed  $0.2 c$ . Third, the X-ray flux is too high to be consistent with the spectral index at radio wavelengths. To support this, we determined the integrated 1.28 GHz flux with a beam size of  $8'' \times 8''$  over the area covering the X-ray filament,  $\sim 25.2'' \times 167.5''$ , giving  $75.5 \pm 13.2 \text{ mJy}$ . The spectral index in the 20 cm band is estimated to be  $-1.18 \pm 0.16$  and is shown in Figure 6.

Instead an inverse-Compton scattering (ICS) scenario seems preferred, in which the X-ray emission is created by the upscattering of seed photons contributed by the bright stellar source located at the northern tip of the X-ray emission. The ICS flux  $F_{\nu_x}$  at frequency  $\nu_x$  is given by

$$\nu_x F_{\nu_x} \approx 0.5 \frac{\nu_1 U_{\nu_1}}{U_B} \nu_0 F_{\nu_0} \quad (1)$$

$\nu_1 U_{\nu_1}$  is the energy density of the seed photons at the peak of the stellar spectrum at frequency  $\nu_1$ ,  $U_B$  is the energy density magnetic field, and  $\nu_0$  is the characteristic frequency of the synchrotron emission of electrons with Lorentz factor  $\gamma \sim (\nu_x / \nu_1)^{1/2}$ .

Adopting a stellar luminosity  $L_* \approx 1 \times 10^6 L_\odot$ , with an SED peaking at  $\nu_1 = 0.5 \mu\text{m}$ , typical of a young massive star, then upscattering to  $h\nu_x \approx 5 \text{ keV}$  is achieved by electrons in the low energy tail with Lorentz factors  $\approx 50$ . The energy density at distance  $d$  from the star is  $U_\nu = L_\nu / (4\pi cd^2)$ . Adopting a synchrotron flux of  $0.1 \text{ Jy}$  at 1.2 GHz and a  $\nu^{-1.4}$  spectrum then  $\nu F_\nu \propto \nu^{-0.4}$  and for our nominal field strength of  $100 \mu\text{G}$  (Yusef-Zadeh, et al. (2005); Yusef-Zadeh & Wardle (2019)), this yields  $0.5\text{--}10 \text{ keV}$  X-ray flux over the extent of the X-ray filament of about  $2 \times 10^{-13} \text{ erg cm}^{-2} \text{ s}^{-1}$ , consistent with the observed X-ray flux. Reducing the adopted magnetic field strength to  $50 \mu\text{G}$  increases the X-ray flux to  $8 \times 10^{-13} \text{ erg cm}^{-2} \text{ s}^{-1}$ .

In this scenario the X-ray emission traces  $\sim 20 \text{ MeV}$  electrons that are injected at (a) the stellar bow shock, and (b) the reconnection point where the oblique filament crosses the north-south filament at point A (see Fig. 6). In both cases the injected particles are carried southwards by the large scale nuclear wind from the inner  $100 \text{ pc}$  of the Galaxy. Inverse Compton scattering off the additional electrons injected at A offsets the  $1/r^2$  decline of the seed photon density with distance from the star and maintains a relatively uniform surface brightness along the north-south filament.

## 4.2 Summary

We have presented a moderate resolution study of the radio structure and spectral index of G0.173-0.42 which consists of two parallel filaments and an oblique filament G0.167-0.405 crossing the parallel filaments. A small portion of one of the two parallel filaments has an X-ray counterpart. Noting the variation in spectral index, sudden brightening and asymmetry of radio and X-ray emission, we argued for an interaction of the oblique filament with one of the two parallel filaments and suggested injection of a new population of relativistic particles due to magnetic field reconnection. The presence of a Galactic center wind produces lopsided profiles through its tendency to push particles away from the injection point. We suggested that the inverse Compton scattering mechanism is more likely to explain the X-ray emission by upscattering of seed photons emitted from a  $10^6 L_\odot$  star located at the

northern tip of the X-ray filament. We argued against the synchrotron mechanism for the X-ray emission due to the short  $\sim 30$  year lifetime of TeV relativistic particles.

## 5 DATA AVAILABILITY

All the data including X-ray, radio and IR data that we used here are available online and are not proprietary. We have reduced and calibrated these data and are available if requested.

## ACKNOWLEDGMENTS

We thank the referee for useful comments. This work is partially supported by the grant AST-0807400 from the National Science Foundation. The MeerKAT telescope is operated by the South African Radio Astronomy Observatory, which is a facility of the National Research Foundation, an agency of the Department of Science and Innovation. IH acknowledges support from the UK Science and Technology Facilities Council [ST/N000919/1], the Oxford Hintze Centre for Astrophysical Surveys which is funded through generous support from the Hintze Family Charitable Foundation, and a visiting Professorship from SARAO. We acknowledge use of the Inter-University Institute for Data Intensive Astronomy (IDIA) data intensive research cloud for data processing. IDIA is a South African university partnership involving the University of Cape Town, the University of Pretoria and the University of the Western Cape. MW thanks the Cherrybrook Research Institute for hospitality. The authors acknowledge the Centre for High Performance Computing (CHPC), South Africa, for providing computational resources to this research project.

## REFERENCES

Asad K. M. B., Girard J. N., de Villers M., Lehmensiek R., Ansah-Narh T., Iheanetu K., Smirnov O., et al., 2019, arXiv, arXiv:1904.07155  
 Bicknell G. V., Li J., 2001, ApJ, 548, L69  
 Briggs D. S., 1995, AAS  
 Chambers E. T., Jackson J. M., Rathborne J. M., Simon R., 2009, ApJS, 181, 360  
 Coelho P. R. T., 2014, MNRAS, 440, 1027  
 Dong H., et al., 2011, MNRAS, 417, 114  
 Engelke C. W., Price S. D., Kraemer K. E., 2006, AJ, 132, 1445  
 Everett J. E., Schiller Q. G., Zweibel E. G., 2010, ApJ, 711, 13  
 Everett J. E., Zweibel E. G., Benjamin R. A., McCammon D., Rocks L., Gallagher J. S., 2008, ApJ, 674, 258  
 Gray A. D., Cram L. E., Ekers R. D., Goss W. M., 1991, Natur, 353, 237  
 Haynes R. F., Stewart R. T., Gray A. D., Reich W., Reich P., Mebold U., 1992, A&A, 264, 500  
 Herold L., Malyshev D., 2019, A&A, 625, A110  
 Heywood I., et al., 2019, Natur, 573, 235  
 Indriolo N., McCall B. J., 2012, ApJ, 745, 91  
 Johnson S. P., Dong H., Wang Q. D., 2009, MNRAS, 399, 1429  
 Lang C. C., Morris M., Echevarria L., 1999, ApJ, 526, 727  
 LaRosa T. N., Nord M. E., Lazio T. J. W., Kassim N. E., 2004, ApJ, 607, 302  
 Law C. J., Yusef-Zadeh F., Cotton W. D., 2008, ApJS, 177, 515  
 Liszt H. S., 1985, ApJ, 293, L65

Le Petit F., Ruaud M., Bron E., Godard B., Roueff E., Languignon D., Le Bourlot J., 2016, A&A, 585, A105  
 Lu F. J., Wang Q. D., Lang C. C., 2003, AJ, 126, 319  
 Lu F. J., Yuan T. T., Lou Y.-Q., 2008, ApJ, 673, 915  
 Martin D. C., Seibert M., Neill J. D., Schiminovich D., Forster K., Rich R. M., Welsh B. Y., et al., 2007, Natur, 448, 780. doi:10.1038/nature06003  
 McMullin J. P., Waters B., Schiebel D., Young W., Golap K., 2007, ASPC, 376, 127  
 Morris M., Yusef-Zadeh F., 1989, ApJ, 343, 703  
 Muno M. P., Baganoff F. K., Brandt W. N., Morris M. R., Starck J.-L., 2008, ApJ, 673, 251  
 Nishiyama S., Tamura M., Hatano H., Kanai S., Kurita M., Sato S., Matsunaga N., et al., 2009, ApJ, 690, 1648  
 Nakashima S., et al., 2013, ApJ, 773, 20  
 Offringa A. R., McKinley B., Hurley-Walker N., Briggs F. H., Wayth R. B., Kaplan D. L., Bell M. E., et al., 2014, MNRAS, 444, 606  
 Offringa A. R., Smirnov O., 2017, MNRAS, 471, 301  
 Oka T., Geballe T. R., Goto M., Usuda T., McCall B. J., 2005, ApJ, 632, 882  
 Oka T., Geballe T. R., Goto M., Usuda T., Benjamin, McCall J., Indriolo N., 2019, ApJ, 883, 54  
 Paré D. M., Lang C. C., Morris M. R., Moore H., Mao S. A., 2019, ApJ, 884, 170  
 Ponti G., et al., 2019, Natur, 567, 347  
 Ramirez S. V., Arendt R. G., Sellgren K., Stolovy S. R., Cotera A., Smith H. A., Yusef-Zadeh F., 2008, ApJS, 175, 147  
 Rosner R., Bodo G., 1996, ApJ, 470, L49  
 Ruszkowski M., Yang H.-Y. K., Zweibel E., 2017, ApJ, 834, 208  
 Sakano M., Warwick R. S., Decourchelle A., Predehl P., 2003, MNRAS, 340, 747  
 Shore S. N., LaRosa T. N., 1999, ApJ, 521, 587  
 Seiradakis J. H., Lasenby A. N., Yusef-Zadeh F., Wielebinski R., Klein U., 1985, Natur, 317, 697  
 Sofue Y., 2020, PASJ, 72, L4  
 Skrutskie M. F., et al., 2006, AJ, 131, 1163  
 Stolovy S., et al., 2006, JPhCS, 54, 176, JPhCS..54  
 Su M., Slatyer T. R., Finkbeiner D. P., 2010, ApJ, 724, 1044  
 Tsuboi M., Kawabata T., Kasuga T., Handa T., Kato T., 1995, PASJ, 47, 829  
 Thomas T., Pfrommer C., Enßlin T., 2020, ApJL, 890, L18  
 Veilleux S., Cecil G., Bland-Hawthorn J., 2005, ARA&A, 43, 769  
 Wilms J., Reynolds C. S., Begelman M. C., Reeves J., Molendi S., Staubert R., Kendziorra E., 2001, MNRAS, 328, L27  
 Yusef-Zadeh F., et al., 2009, ApJ, 702, 178  
 Yusef-Zadeh F., Hewitt J. W., Cotton W., 2004, ApJS, 155, 421  
 Yusef-Zadeh F., PhD thesis, Columbia University, 1986  
 Yusef-Zadeh F., Morris M., Chance D., 1984, Natur, 310, 557  
 Yusef-Zadeh F., Morris M., Lasenby A. N., Seiradakis J. H., Wielebinski R., 1990, IAUS, 140, 373, IAUS..140  
 Yusef-Zadeh F., Wardle M., Muno M., Law C., Pound M., 2005, AdSpR, 35, 1074  
 Yusef-Zadeh F., Wardle M., 2019, MNRAS, 490, L1  
 Yusef-Zadeh F., Wardle M., Parastaran P., 1997, ApJ, 475, L119  
 Zhang S., et al., 2020, ApJ, 893, 3  
 Zhang S., Wang D. Q., Clavel M., 2020, American Astronomical Society meeting #236, Bulletin of the American Astronomical Society, Vol. 52, No. 3  
 Zhang S., et al., 2014, ApJ, 784, 6  
 Zweibel E. G., 2017, PhPl, 24, 55402

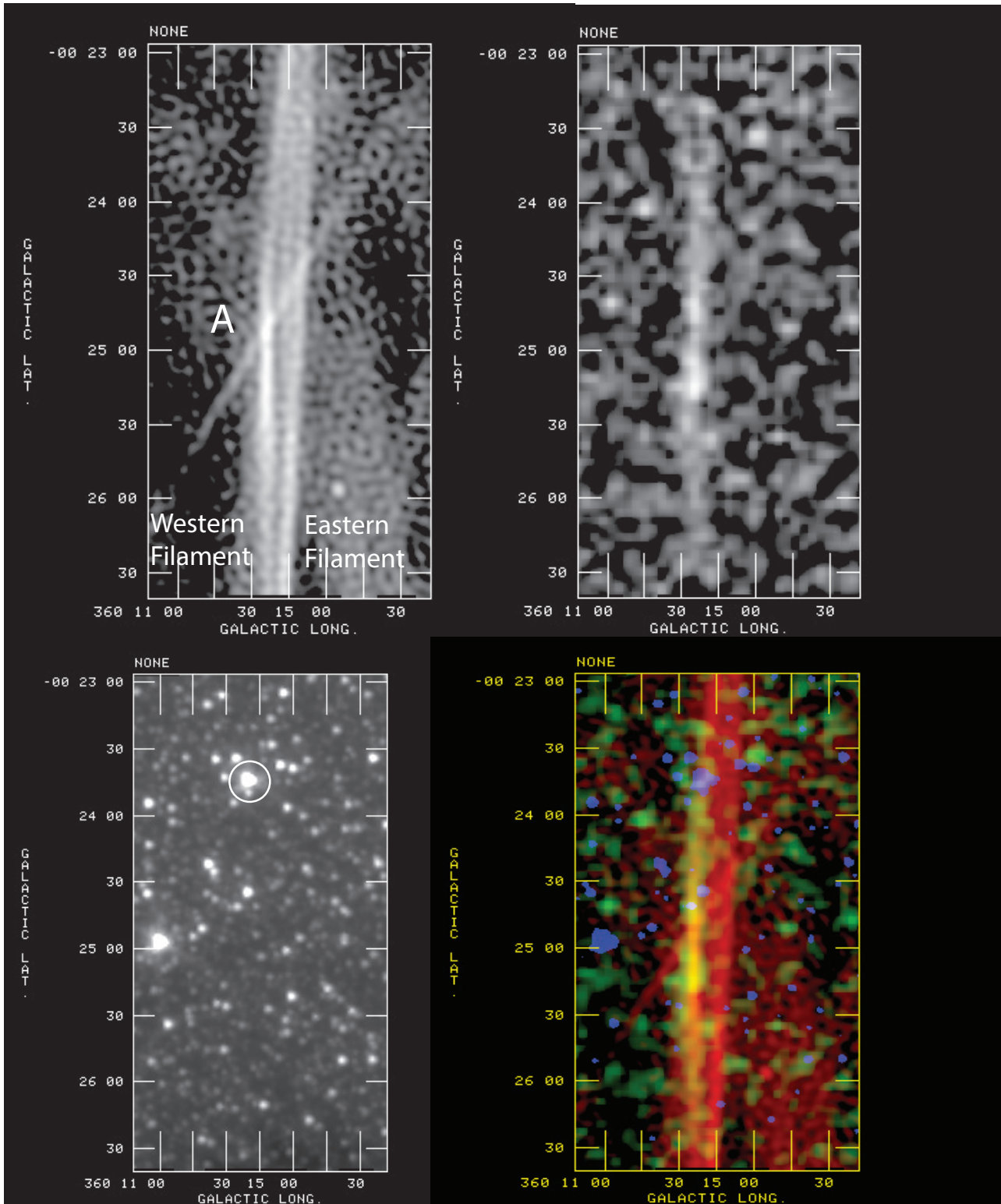


**Figure 1.** *a*(Top Left) A grayscale MeerKAT image at 20 cm showing an oblique filament crossing two parallel filaments at position A with a resolution of  $\sim 4'' \times 4''$ . The eastern and western filaments are labeled. Note that diffuse radio emission surrounds the filaments. *b*(Top Right) A *Chandra* X-ray image integrated between 2-8 keV shows a single filament coincident with the eastern radio filament but its northern extension from position A deviates to the NW in the direction away from the eastern radio filament. A circle shows the position of the bright star shown in (c). *c*(Bottom Left) A 3.6  $\mu\text{m}$  image of G0.173-0.42 taken with *Spitzer*/IRAC of *Spitzer*. A bright saturated star is located where the X-ray filament splits into two components. The bright saturated star is marked with a circle. *d*(Bottom Right) A composite RGB color image of the G0.173-0.42 filament at radio (R) and X-ray (G) superimposed on an IRAC image (B) at 3.6  $\mu\text{m}$ .

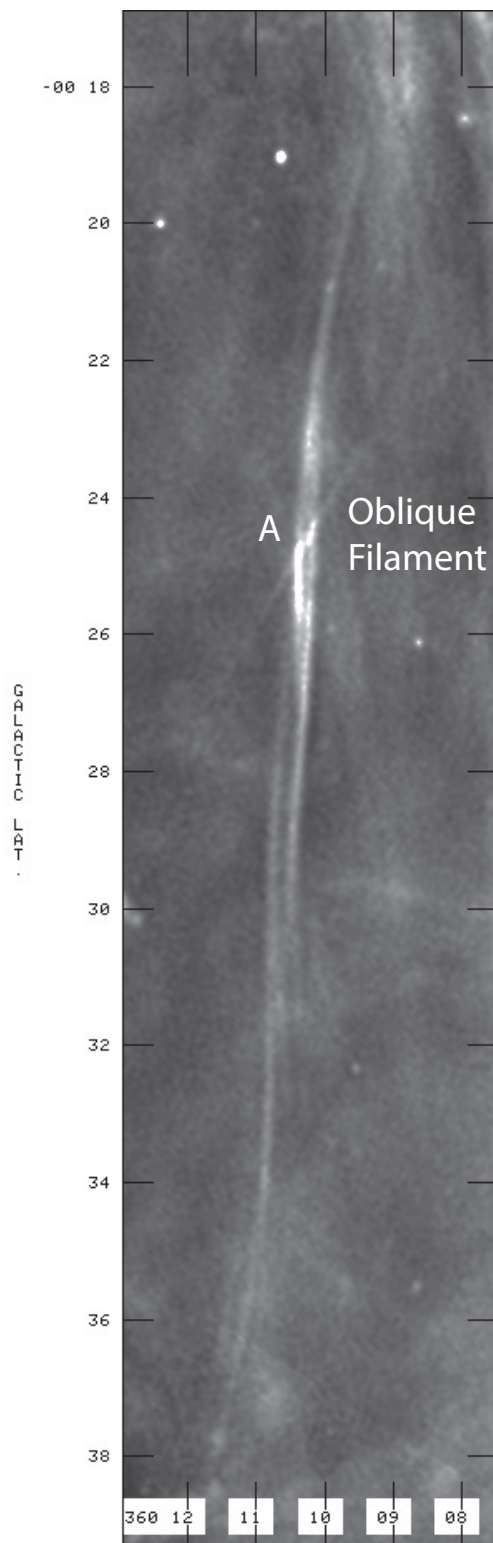


**Figure 2.** A 1.28 GHz image of a network of parallel filaments, the brightest portion of which includes G0.173-0.42. The range of intensity ranges between  $-5 \times 10^{-5}$  and  $3 \times 10^{-4}$  Jy beam $^{-1}$  and the spatial resolution is  $\sim 6''$ .

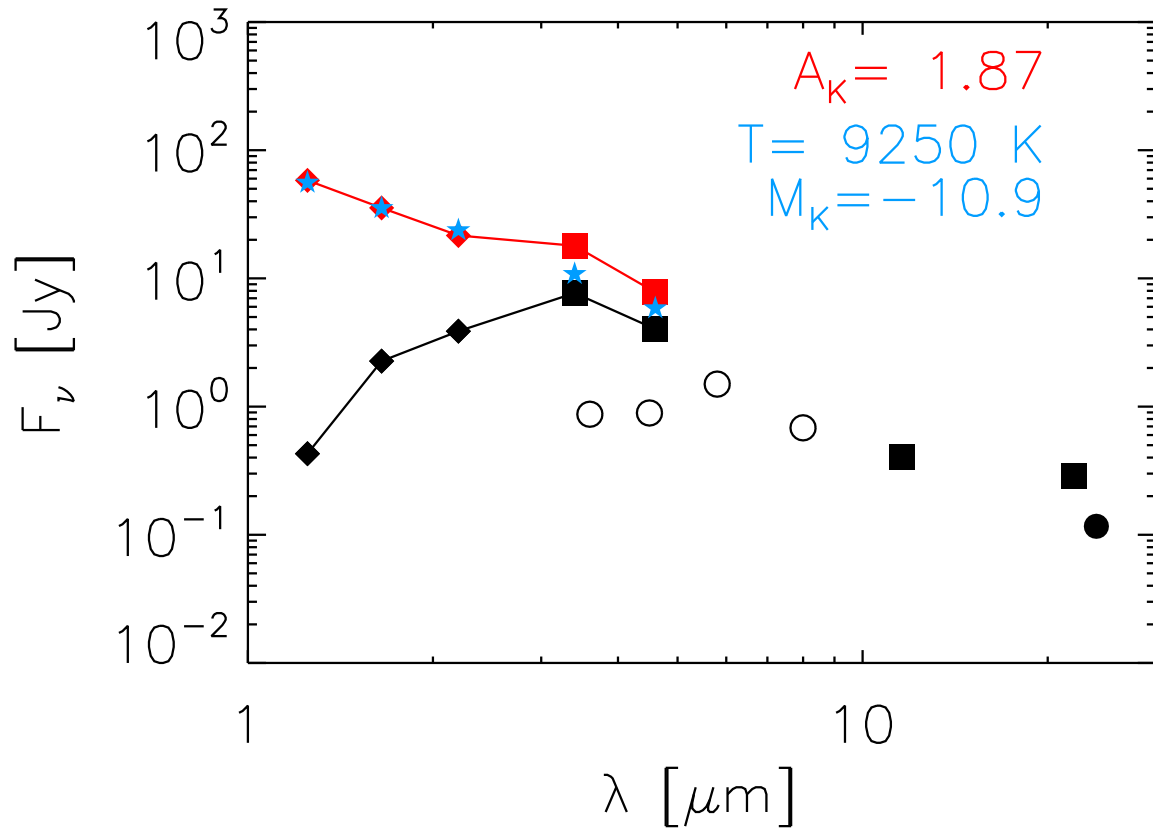


**Figure 3.** A spectral energy distribution (SED) of the brightest star in the cluster at the northern tip of the X-ray filament. Observed flux densities are designated by black symbols: 2MASS (diamonds), IRAC (likely affected by saturation, open circles), MIPS (filled circle) and *WISE* (squares). Red symbols indicate the extinction-corrected SED derived from a weighted fit between the 2MASS + *WISE* data and the [Coelho \(2014\)](#) stellar models. The fit indicates an extinction of  $A_K = 1.87$  mag, and a stellar atmosphere model (blue stars) with  $T = 9250$  K and an absolute K band magnitude of  $M_K = -10.9$ .

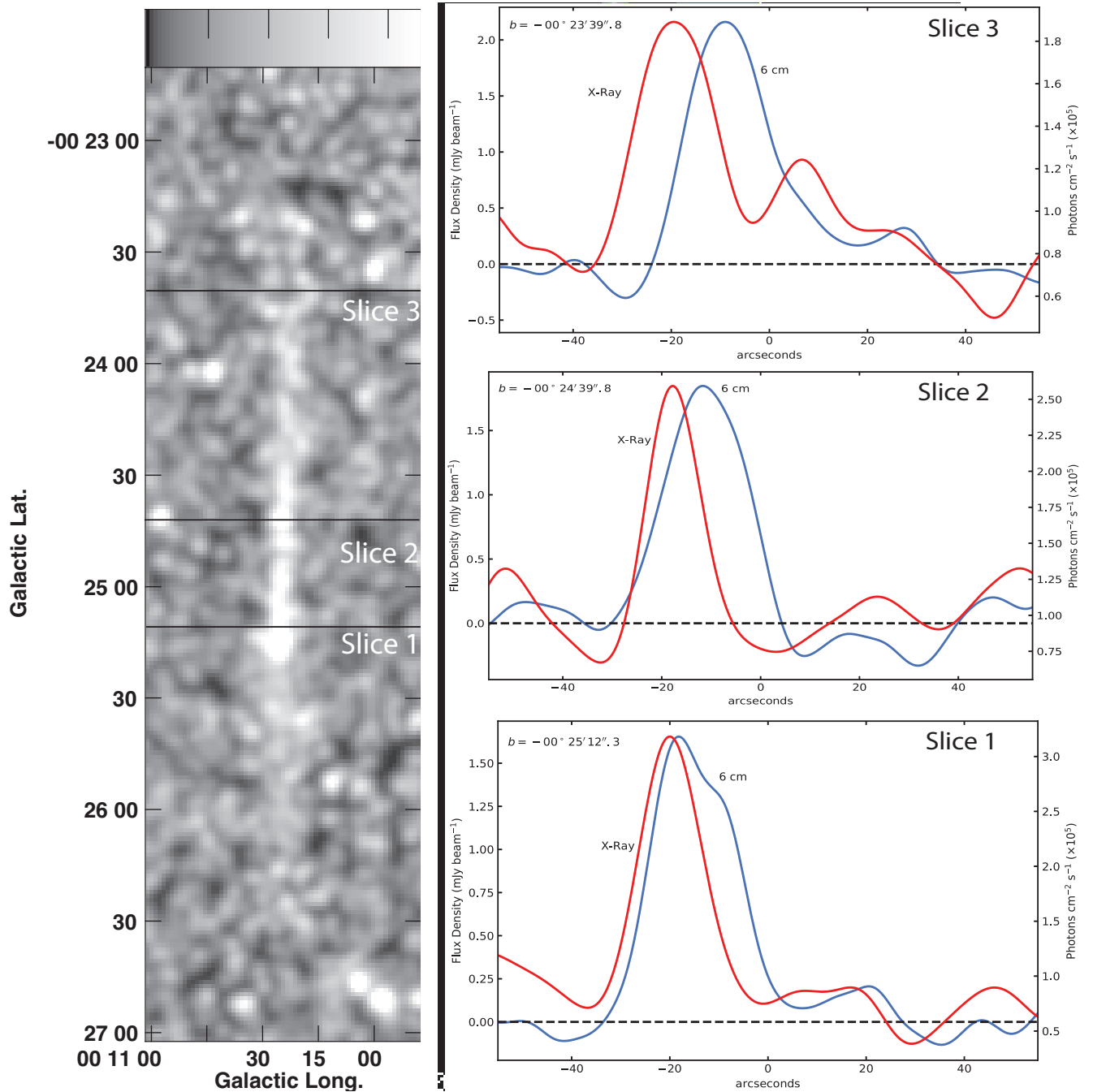


**Figure 4.** *a* (Left) Lines on the X-ray image show the locations of profile measurements. Only the eastern filament of G0.173-0.42 appears in X-rays. The parallel western radio filament is  $10''$  away. *b* (Right three panels) The slice profiles show that the eastern radio filament shows an X-ray counterpart. The X-ray flux is integrated between 1.5 and 5 keV. Both radio and X-ray data are convolved to a Gaussian beam  $11''.95 \times 8''.69$  with position angle (PA)  $72^\circ.55$ . Linear fits were used to subtract background emission from these profiles.

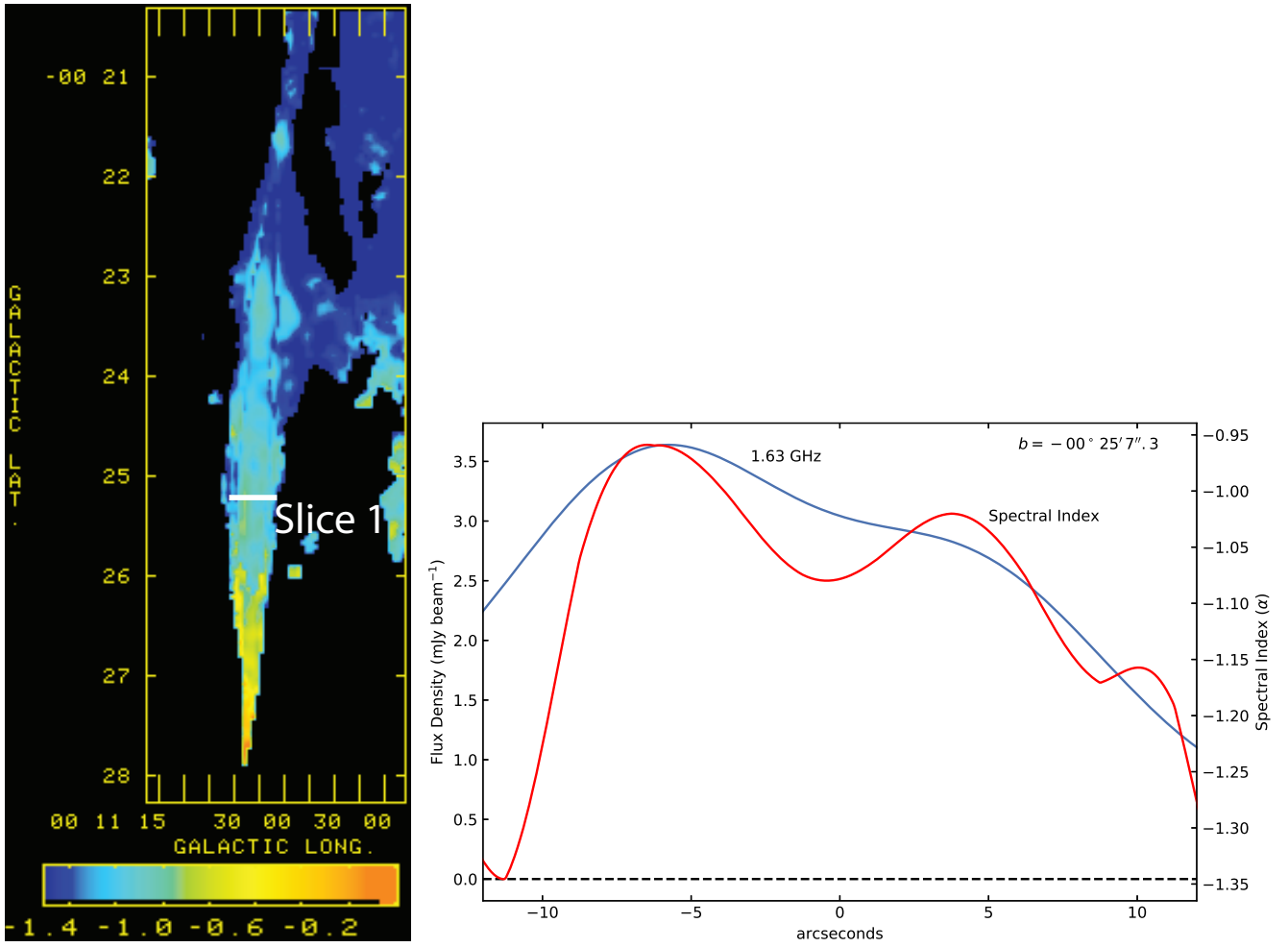


**Figure 5.** *a(Left)* A spectral index image based on 15 MeerKAT sub-bands within the 20 cm band between 0.8 to 1.6 GHz convolved with an  $8''$  resolution. *b(Right)* The spectral index (red-line) determined from a slice cutting across the width of the filament, as labeled by a horizontal line segment on Figure 5a. The 1631.6 MHz intensity profile (blue line) of the filaments is shown for reference.

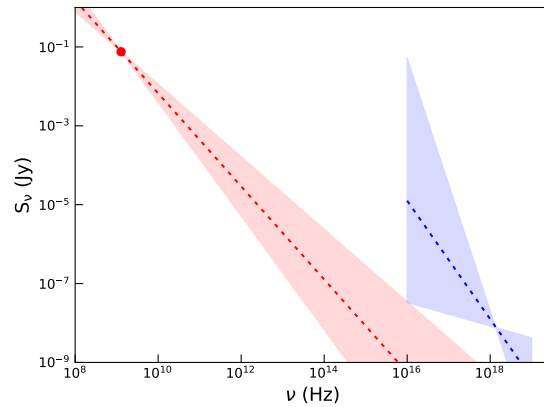


**Figure 6.** The integrated flux densities of the entire X-ray filament and the corresponding radio counterpart at 1.28 GHz. The extrapolations of the radio and X-ray spectra are shown in red and blue, respectively, with dashed lines and shaded regions indicate the best fit spectral indices and their 90% confidence intervals. The 90% confidence level on the radio spectral index is computed from  $-1.18 \pm 0.16$  with a flux density of 75.5 mJy. took them from the text. The X-ray photon index  $\Gamma = 2.5^{+1.7}_{-1.2}$  with a 2-10 keV fluxes (unabsorbed)  $2.0^{+2.5}_{-0.5} \times 10^{-13}$  ergs  $s^{-1}$  are used to determine the best fit spectral index to X-ray data.

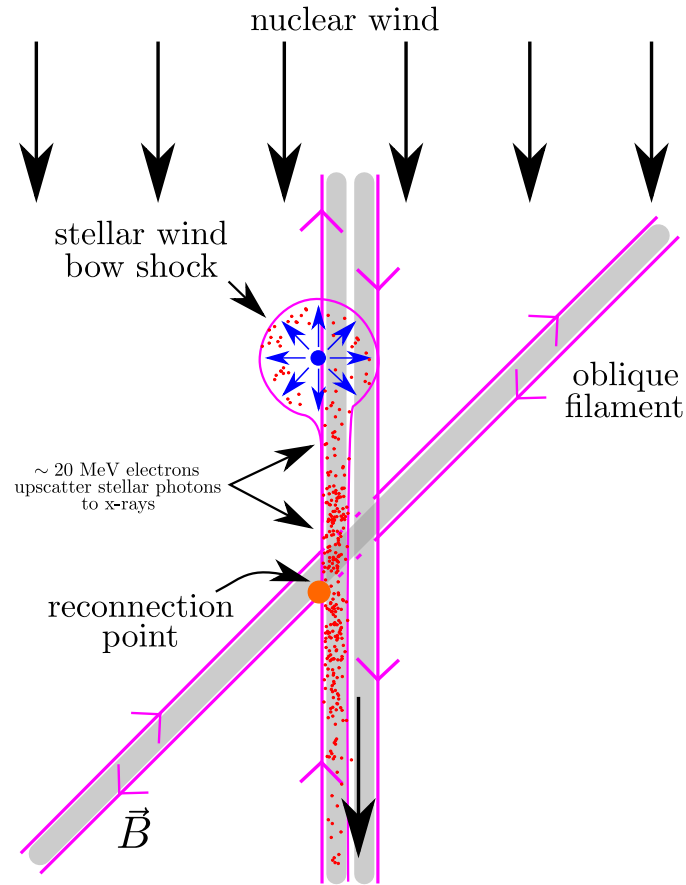


**Figure 7.** A schematic diagram of an oblique filament crossing two parallel filaments, producing a new population of relativistic particles. Cosmic ray particles from the nuclear wind and the reconnection point interact in two locations with the seed photons of a luminous mass-losing star and produce X-ray emission due to ICS, as shown in red.